Journal of Nanofluids
Vol. 14, pp. 394–410, 2025
(www.aspbs.com/jon)

ARTICLE

Numerical Simulation of Hydromagnetic Flow and Heat Transfer of Hybrid Nanofluid Over a Rotating Disk in a Porous Medium with Slip Conditions and Hall Current: A Buongiorno Model Approach

Folarin Oluwaseun[1,*] and Titilayo M. Agbaje[2,3]

[1]*School of Mathematics, Statistics, and Computer Science, University of the KwaZulu-Natal, Private Bag X01, Scottsville, Pietermaritzburg, 3209, South Africa*
[2]*School of Computer Science and Applied Mathematics, University of the Witwatersrand, Johannesburg, Private Bag 3, Braamfontein, 2050, South Africa*
[3]*Center for Sustainable Smart Cities, Department of Mathematical and Physical Sciences, Central University of Technology, Free State, Private Bag X20539, Bloemfontein, 9300, South Africa*

This study presents a compelling numerical simulation of hydromagnetic flow and heat transfer in a hybrid nanofluid composed of carbon nanotubes (CNTs) and iron oxide (Fe_3O_4) over a rotating disk within a porous medium. Driven by the urgent need to enhance thermal performance in next-generation energy and cooling systems, the investigation integrates advanced physical mechanism of Hall currents, velocity slip, thermal jump conditions, and the Buongiorno model to realistically capture transport behavior under extreme engineering conditions. The nonlinear governing equations are computed using the overlapping spectral quasi-linearization method, a highly accurate and efficient computational technique. The results uncover rich physical insights: magnetic fields suppress flow via Lorentz forces while significantly enhancing thermal energy transfer through Joule heating. Porosity and slip conditions markedly affect momentum diffusion and boundary layer development, while nanoparticle effects such as Brownian motion, thermophoresis, and shape factors critically shape thermal conductivity and concentration distributions. Importantly, multi-walled carbon nanotubes (MWCNT) demonstrate superior thermohydraulic performance over their single-walled counterparts, highlighting their promise for high-efficiency thermal systems. These findings offer practical design implications for thermal management technologies, energy harvesting systems, and microfluidic devices, advancing both the scientific understanding and applied potential of hybrid nanofluid dynamics.

KEYWORDS: Binary Nanofluids, Hybrid Nanofluid, Activation Energy, Overlapping Spectral Quasi-Linearization, Entropy Generation Optimization, Nanoparticle Shape Factor, Porosity, Rotating Disk.

1. INTRODUCTION

The study of fluid flow over rotating disks has gained considerable attention due to its numerous applications in engineering and industrial processes, such as boundary layer control in turbine rotors, computer hard disk drives, centrifugal pumps and rotating machinery.[1] Pioneering work by Kármán[2] established the analytical solution for a steady, incompressible laminar flow driven by an infinite rotating disk in a viscous fluid. Subsequent studies have extended this analysis by incorporating complexities such as porous media, Mechanisms of heat transmission, and the presence of nanoparticles.[3–6] For instance, Sparrow and Gregg[7] examined the heat transfer characteristics of a rotating disk in the presence of a magnetic field, highlighting the impact of the magnetic field on flow behavior and thermal properties. Mustafa[8] investigated the magnetohydrodynamic (MHD) flow of a nanofluid over a rotating disk, incorporating the Buongiorno model and considering partial slip conditions. Meanwhile, Yin et al.[9] focused on the heat transfer mechanisms associated with fluid flow over a radially stretchable rotating disk. In recent years, the use of nanofluids engineered by dispersing nanometer-sized particles into base fluids has shown significant promise in enhancing thermal and flow properties.

*Author to whom correspondence should be addressed.
Email: folarino987@yahoo.com
Received: 24 January 2025
Accepted: 12 May 2025

Hybrid nanofluids, which combine different types of nanoparticles, offer further improvements in thermal conductivity, viscosity, and heat transfer rates compared to conventional nanofluids. Researchers have demonstrated that hybrid nanofluids exhibit enhanced thermal conductivity and improved heat transfer performance.[10–12] For instance, Suresh et al.[13] investigated the thermal properties of hybrid nanofluids containing Al_2O_3 and CuO nanoparticles and found a notable increase in thermal conductivity compared to binary nanofluids. Similarly, Murshed et al.[14] highlighted the potential of SWCNT and Fe_3O_4 hybrid nanofluids in improving thermal properties and heat transfer rates. Ahmadian et al. [15] carried out an extensive investigation into the unsteady flow of hybrid nanofluids, focusing on the simultaneous transfer of mass and energy over a non-uniformly spinning disk. They employed parametric continuation method (PCM) to analyze the flow behavior. Their research highlighted the significant impact of incorporating nanomaterials into the primary fluid medium, which is particularly beneficial for applications in hyperthermia treatment, power generation, and the microfabrication process. In a separate study, Shahid et al.[16] explored the effect of gyrotactic microorganisms on the magnetohydrodynamic (MHD) flow of nanofluids. They utilized the local linearization method to understand these interactions and their influence on the flow dynamics.

Exploring the behavior of nanofluid flow in the presence of a magnetic fields holds significant importance in various engineering applications. When an electric charge moves, it generates a magnetic field, which is the region around a magnet where magnetic forces can be detected. The incorporation of a magnetic field into nanofluid flow enhances the analysis of thermal transport and magnetohydrodynamic effects. This interaction induces Lorentz forces due to the fluid's electrical conductivity, thereby modifying its flow dynamics and temperature distribution. These insights are crucial for Practical implementations like pharmaceutical delivery systems and the control of micro-scale flows in microfluidic circuits and metallurgical processes especially in the purification they are given as: of molten metals. Pavlov[17] was motivated by these industrial applications and began examining the Conductive fluid flow near the boundary layer caused by an elastically deforming panel. Rashidi et al.[18] formulated a mathematical model to investigate the impact of thermophoretic diffusion and Dufour effects on a time-invariant magnetohydrodynamic (MHD) flow generated by a rotating porous disk in the presence of an external magnetic field. Hayat et al.[19] investigated the impact of hydromagnetic flow between two rotating disks subjected to a magnetic field. In their study, Khan et al.[20] applied the Bvp4C numerical solver, incorporating a shooting method, to explore the impact of Heat waves and the consequences of heat sources and sinks on the behavior of nanofluid circulation and heat transfer occurring between two rotating coaxial disks. Ahmed et al.[21] explored the unsteady thin film flow of Maxwell nanofluids over a rotating disk using the Buongiorno model, employing the Bvp4C finite difference method for their analysis. Hall currents, arising from the movement of the electrified particles in a magnetic field, add complexity to the flow dynamics of conducting fluids. These currents can modify the flow structure and heat transfer characteristics in significant ways. Studies such as those by Raptis and Perdikis[22] have examined the impact of Hall currents on MHD flow, finding that they are vital in establishing the overall behavior of the fluid flow. In the context of nanofluid flows over rotating disks, the presence of Hall currents necessitates a detailed analysis to accurately predict flow and thermal patterns.[23]

The interest of scientists has been drawn to heat transfer in carbon-based nanofluids across various technological fields. Carbon nanotubes (CNTs) are made up of cylindrically organized carbon atoms, have been widely studied due to their exceptional thermophysical, chemical, electrical, and mechanical properties. These characteristics make CNTs an ideal choice as nanoparticles in base fluids. The unique features of CNTs such as an extensive outer surface, tubular shape, chemical stability, hardness, and nanoscale dimensions compared to other nanoparticles offer distinct advantages in heat transfer applications.

Carbon nanotubes (CNTs) are classified according to the quantity of graphene layers they contain, resulting in two main types: single-walled (SWCNTs) and multi-walled (MWCNTs) nanotubes. These forms exhibit varying properties that influence their performance in nanofluids. Khan et al.[24] reviewed the thermodynamic aspect of entropy generation in a rotating frame with CNT-based MHD flow, demonstrating how the inclusion of CNTs contributes to improved heat transfer efficiency in rotating systems. Anuar et al.[25] examined the influence of magnetohydrodynamic (MHD) forces on steady, two-dimensional flow of CNTs over a nonlinear surface, demonstrating the significant impact of MHD on the induced flow characteristics. Mahanthesh et al.[26] examined the movement of carbon nanofluids over a rotating disk, emphasizing the effects of rotation on heat transfer properties and providing insights into the behaviour of nanofluids in rotational systems, which are common in engineering applications. Gul et al.[27] developed a computational framework to evaluate and contrast the thermal performance of hybrid and conventional nanofluids over a stretching surface. The findings highlighted that hybrid nanofluids comprising multiple nanoparticle types offer improved heat transfer characteristics compared to single-type nanofluids.

Incorporating a porous medium into fluid flow studies is critical for modeling real-world scenarios where the fluid interacts with permeable materials. The Darcy-Forchheimer model is commonly used to describe such flows, taking kinetic and viscous interactions into consideration.

Studies have shown that the presence of a porous materials can have substantial effects on the properties of nanofluid movement and thermal transmission. For example, Makinde and Aziz[28] explored the behavior of nanofluid flow in the boundary layer region along a stretching sheet in a porous material, highlighting the complex interactions between the fluid and the porous structure. Activation energy is a fundamental concept in chemistry and physics, representing the minimum energy required for a reaction to occur. Activation energy is the minimum energy input to activate a chemical reaction. Svante Arrhenius introduced the concept of activation energy in 1889. The Arrhenius equation quantitatively describes the relationship between the reaction rate and the activation energy. Initially, in a chemical reaction system, the activation energy may be considered negligible or zero under certain assumptions. Activation energy refers to the least amount of energy needed for reactant molecules to initiate a chemical reaction and be converted into products, a reaction proceeds once this energy threshold is overcome. According to Maxwell's distribution, only those atoms with energy higher than this barrier can surpass it, hence the activation energy is considered the Extent of the activation barrier. In the context of nanofluids, activation energy pertains to the energy needed for the nanoparticles to overcome interfacial forces and interact with the base fluid. This interaction significantly influences the thermophysical properties of the nanofluid, such as thermal conductivity, viscosity, and heat capacity. Hayat et al.[29] Explored entropy production in the motion of Ree-Eyring nanofluids between rotating disks, with Arrhenius activation energy integrated into the formulation. The nonlinear governing equations were tackled using a semi-analytical solution method. Similarly, Kumar et al.[30] explored the entropy production mechanisms in nanofluid flow over a stretching surface, factoring in activation energy. Additionally, Khan et al.[31] examined the entropy production in magnetohydrodynamic radiative flow of nanomaterials, considering an activation energy-driven chemical process of the second order.

Building on the existing literature, this research examine the steady-state movement of a nanofluid combination-consisting of carbon nanotubes (CNTs) and Fe_3O_4 above a spinning disk embedded in a fluid substance, a configuration that is highly relevant for advanced engineering applications such as cooling systems, energy conversion devices, and chemical reactors. The rotating disk, subjected to a uniform magnetic field perpendicular to its surface, simulates real-world scenarios where magnetic control of fluid flow is critical. By incorporating Hall currents and partial slip conditions, this study captures complex boundary interactions that are often overlooked but are cardinal for optimizing the interpretation of nanofluid-based systems in industrial processes. Furthermore, the use of the Buongiorno model enables a detailed examination of the consequences of heat exchange and Brownian motion offering deeper insights into the thermal and mass transport characteristics of the hybrid nanofluid. The numerical solution is obtained using the overlapping spectral quasilinearization method, which enhances computational efficiency and accuracy, enabling the simulation of larger domains with fewer grid points. This research not only forge ahead the understanding of hybrid nanofluid dynamics but also provides practical contributions to the design and optimization of high-performance thermal systems, underscoring its engineering relevance and unique impact in the field.

2. PRACTICAL DESCRIPTION OF THE PROBLEM

In the framework of this research, we investigate the movement of an electrically performing hybrid nanofluid composed of carbon nanotubes (CNTs) and iron oxide Fe_3O_4 over a spinning disk with the following assumptions:

- The movement is assumed to be steady and occurs within a porous medium, typical in numerous engineering usage, such as filtration systems and geothermal reservoirs, where fluid interactions with porous materials significantly affect the overall flow behavior.
- The thermally insulated rotating disk is situated at $z = 0$ and it rotates about z −axis with an angular velocity of Ω.

- A consistent magnetic force, B_0 is utilized perpendicular to the surface of the rotating disk. Including this term is crucial for simulating environments where magnetic fields control fluid flow, such as in electromagnetic pumps and cooling systems for nuclear reactors.
- Presence of Hall current, $m = \tau_e \omega_e$, where ω_e represents the electron frequency and τ_e represents the electron collision. This effect becomes significant in cases involving strong magnetic fields and high electrical conductivities, where the deflection of charged particles impacts the nanofluid's flow and heat transfer characteristics. This term is essential for accurately capturing the fluid's electrodynamics under such conditions.
- The Buongiorno model is adopted to take into consideration impacts of thermophoresis and Brownian motion resulting from the presence of nanoparticles.
- Slip boundary conditions are employed in this study to account for the partial adherence of fluid particles to the rotating disk surface, which becomes significant when dealing with micro- and nano-scale flows or surfaces with low adhesion. Physically, this implies that the fluid does not strictly follow the classical no-slip condition; instead, it experiences a finite velocity relative to the surface due to weak intermolecular interactions. This condition is particularly relevant When the typical roughness height is negligible compared to the boundary layer depth, as is often

the case in engineered porous media, high-speed rotating systems, or microfluidic devices. Incorporating partial slip allows for a more realistic representation of wall-fluid interactions under such circumstances and helps to better predict flow behaviour and shear stress distributions near the surface.

- The movement belongs to the cylindrical positional framework $(r, \emptyset, z)$, with $\tilde{v}_1$, $\tilde{v}_2$ and $\tilde{v}_3$ in r, $\emptyset$ and z directions.
- T_{ws}, T_∞, C_{ws} and C_∞ are temperatures and concentrations on the disk interface and in the region extending outward as seen in the flow geometry depicted in Figure 1.

Based on these assumptions, we define the flow equations following[8, 32]

$$\frac{\partial \tilde{v}_1}{\partial r} + \frac{\partial \tilde{v}_3}{\partial r} = -\frac{\tilde{v}_1}{r} \tag{1}$$

$$\left.\begin{aligned} &\rho_{\text{hnf}}\left(\tilde{v}_1\frac{\partial \tilde{v}_1}{\partial r} - \frac{(\tilde{v}_2)^2}{r} + \tilde{v}_1\frac{\partial \tilde{v}_1}{\partial z}\right) + \frac{\partial P}{\partial r} \\ &= \mu_{\text{hnf}}\left(\frac{\partial^2 \tilde{v}_1}{\partial r^2} + \frac{1}{r}\frac{\partial \tilde{v}_1}{\partial r} - \frac{\tilde{v}_1}{r^2} + \frac{\partial^2 \tilde{v}_1}{\partial z^2}\right) \\ &\frac{\sigma_{\text{hnf}}B_0}{(1+m^2)}(\tilde{v}_1 - m\tilde{v}_2) - \frac{\mu_{\text{hnf}}}{k^{**}}\tilde{v}_1 \end{aligned}\right\} \tag{2}$$

$$\left.\begin{aligned} &\rho_{\text{hnf}}\left(\tilde{v}_1\frac{\partial \tilde{v}_2}{\partial r} + \frac{\tilde{v}_1\tilde{v}_2}{r} + \tilde{v}_3\frac{\partial \tilde{v}_2}{\partial z}\right) \\ &= \mu_{\text{hnf}}\left(\frac{\partial^2 \tilde{v}_2}{\partial r^2} + \frac{1}{r}\frac{\partial \tilde{v}_2}{\partial r} - \frac{\tilde{v}_2}{r^2} + \frac{\partial^2 \tilde{v}_2}{\partial z^2}\right) \\ &\frac{\sigma_{\text{hnf}}B_0}{(1+m^2)}(\tilde{v}_2 + m\tilde{v}_1) - \frac{\mu_{\text{hnf}}}{k^{**}}\tilde{v}_2 \end{aligned}\right\} \tag{3}$$

$$\begin{aligned} &\rho_{\text{hnf}}\left(\tilde{v}_1\frac{\partial \tilde{v}_3}{\partial r} + \tilde{v}_3\frac{\partial \tilde{v}_3}{\partial z}\right) + \frac{\partial P}{\partial z} \\ &= \mu_{\text{hnf}}\left(\frac{\partial^2 \tilde{v}_3}{\partial r^2} + \frac{1}{r}\frac{\partial \tilde{v}_3}{\partial r} + \frac{\partial^2 \tilde{v}_3}{\partial z^2}\right) \end{aligned} \tag{4}$$

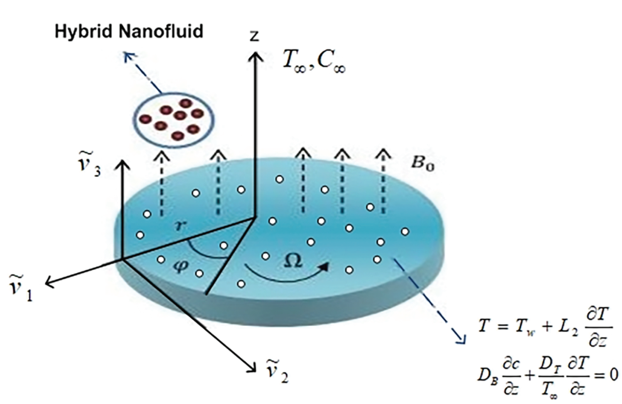

Fig. 1. Illustration of the model's flow configuration.

$$\left.\begin{aligned} \tilde{v}_1\frac{\partial T}{\partial r} + \tilde{v}_3\frac{\partial T}{\partial z} &= \frac{k_{\text{hnf}}}{(\rho C_p)_{\text{hnf}}}\left(\frac{\partial^2 T}{\partial r^2} + \frac{\partial^2 T}{\partial z^2} + \frac{1}{r}\frac{\partial T}{\partial r}\right) \\ &+\delta^*\left[D_B\left(\frac{\partial T}{\partial r}\frac{\partial C}{\partial r} + \frac{\partial T}{\partial z}\frac{\partial C}{\partial z}\right)\right] \\ &+\delta^*\left[\frac{D_T}{T_\infty}\left\{\left(\frac{\partial T}{\partial r}\right)^2 + \left(\frac{\partial T}{\partial z}\right)^2\right\}\right] \\ &-\frac{\partial q_r}{\partial z} \end{aligned}\right\} \tag{5}$$

$$\begin{aligned} \left(\tilde{v}_1\frac{\partial C}{\partial r} + \tilde{v}_3\frac{\partial C}{\partial z}\right) &= D_B\left(\frac{\partial^2 C}{\partial r^2} + \frac{1}{r}\frac{\partial C}{\partial r} + \frac{\partial^2 C}{\partial z^2}\right) \\ &+ \frac{D_T}{T_\infty}\left(\frac{\partial^2 T}{\partial r^2} + \frac{1}{r}\frac{\partial T}{\partial r} + \frac{\partial^2 T}{\partial z^2}\right) \end{aligned} \tag{6}$$

The boundary conditions defined as[8, 32] are:

$$\left.\begin{aligned} &\tilde{v}_1 = L^*_1\left(\frac{\partial \tilde{v}_1}{\partial z}\right); \quad \tilde{v}_2 = r\Omega + L^*_1\left(\frac{\partial \tilde{v}_2}{\partial z}\right); \quad \tilde{v}_3 = 0; \\ &T = T_{ws} + L^*_2\left(\frac{\partial T}{\partial z}\right); \quad D_B\frac{\partial C}{\partial z} + \frac{D_T}{T_\infty}\frac{\partial C}{\partial z} = 0; \quad \text{at } z = 0, \\ &\tilde{v}_1 \to 0; \quad \tilde{v}_2 \to 0;\ T \to T_\infty; \\ &C \to C_\infty \quad \text{as } z \to \infty \end{aligned}\right] \tag{7}$$

Where L^*_1 is the wall slip coefficient, L^*_2 is the temperature slip coefficient, μ_{hnf}, ρ_{hnf}, K_{hnf}, and $(\rho C_p)_{\text{hnf}}$, these terms correspond to the dynamic viscosity, electrical conductivity, density, thermal conductivity, and the volumetric heat capacity of the hybrid nanofluid. The radiative heat flux, q_r, is defined according to the expression in Ref. [33]

$$q_r = -\frac{4\sigma^*}{3k^*}\frac{\partial T^4}{\partial z}$$

In this context, σ^* denotes Boltzmann's constant, while k* represents the absorption coefficient.

We define the hybrid nanofluid properties with the physical properties displayed in Table I. These definitions are in accordance with Ref. [34] as:

$$\mu_{\text{hnf}} = \frac{\mu_f}{(1-\varphi)^2}$$

$$\frac{\rho_{\text{hnf}}}{\rho_f} = \left[1 - \varphi + \varphi\left(\frac{\rho_s}{\rho_f}\right)\right]$$

Table I. Thermophysical features of H_2O, Fe_3O_4, and CNTs.

Physical features	H_2O	Fe_3O_4	SWCNT	MWCNT
Density, ρ (Kgm^{-3})	997.1	5200	2600	1600
Heat capacitannce, C_p (JK^{-1})	4179	670	425	796
Thermal conductivity, k $(\text{Wm}^{-1}\ \text{K}^{-1})$	0.613	6.0	6600	3000
Electrical conductivity, σ (Sm^{-1})	0.05	250000	10^7	10^7

ARTICLE

$$\frac{(\rho C_p)_{\text{hnf}}}{(\rho C_p)_f} = \left[1 - \varphi + \varphi\left(\frac{(\rho C_p)_s}{(\rho C_p)_f}\right)\right]$$

$$\frac{k_{\text{hnf}}}{k_f} = \frac{1+\varphi_2+2\varphi_2\left(k_2/k_2 - k_{bf}\right)\ln\left(k_2+k_{bf}/2k_{bf}\right)}{1+\varphi_2+2\varphi_2\left(k_{bf}/k_2 - k_{bf}\right)\ln\left(k_2+k_{bf}/2k_{bf}\right)}$$

$$\frac{k_{bf}}{k_f} = \frac{k_1+(n-1)k_f-(n-1)\varphi_1\left(k_f-k_1\right)}{k_1+(n-1)k_f-\varphi_1\left(k_f-k_1\right)}$$

$$\frac{\sigma_{\text{hnf}}}{\sigma_{bf}} = 1+\frac{3\varphi_2\left(\sigma_2/\sigma_{bf}-1\right)}{\left(\sigma_2/\sigma_{bf}+2\right)\left(\sigma_2/\sigma_{bf}-1\right)\varphi_2}$$

$$\frac{\sigma_{bf}}{\sigma_f} = \frac{\sigma_{\text{Fe}_3\text{O}_4}+(n-1)\sigma_f-(n-1)\varphi_1\left(\sigma_f-\sigma_{\text{Fe}_3\text{O}_4}\right)}{\sigma_{\text{Fe}_3\text{O}_4}+(n-1)\sigma_f+\varphi_1\left(\sigma_f-\sigma_{\text{Fe}_3\text{O}_4}\right)}$$

In this case, n is the shape factor of Fe_3O_4 nanoparticle and it is given as $n = 3/\psi$, where ψ is the shape factor parameter. For the current study, we consider Fe_3O_4 to assume spherical shape ($\psi = 1.0$), cylindrical shape ($\psi = 0.61$) and platelet shape ($\psi = 0.53$). φ_1 and φ_2 are the nanoparticle fractions of Fe_3O_4 and CNTs respectively. φ, ρ_s, ρ_f, and $\left(C_p\right)_s$ are used to define the hybrid nanofluid viscosity, density, and heat capacity in terms of the nanoparticle weights rather than the crystalline particles' typical volumetric concentration

and they are given as:

$$\rho_s = \frac{(\rho_1 \times w_1)+(\rho_2 \times w_2)}{w_1+w_2}$$

$$\varphi = \frac{w_1 + w_2/\rho_s}{w_1 + w_2/\rho_s + w_f/\rho_f}$$

$$(C_p)_s = \frac{\left((C_p)_1 \times w_1\right)+\left((C_p)_2 \times w_2\right)}{w_1+w_2}$$

To address the order of partial differential Eqs. (1)–(6) numerically, subject to condition (7), we employ the boundary layer approach via the introduction of similarity transformations. This approach is chosen due to its proven effectiveness in simplifying complex fluid flow problems while retaining the essential physical characteristics, particularly in scenarios involving rotating disks and magnetic fields. This approach has been successfully applied in numerous studies, such as Refs. [8, 32], providing accurate and computationally efficient solutions. In this study, the BL approach allows for the detailed examination of near-wall effects, such as slip conditions and thermal gradients, which are critical in understanding the nanofluid behavior. These Transformational techniques are adopted to create an analogous Nonlinear ODEs obtained through the reduction of the governing nonlinear PDEs. The overlapping grid spectral quasilinearization approach is then used to solve the resultant system.

The transformations are given as:

$$\left.\begin{aligned} &\eta = y\sqrt{\frac{2\Omega}{\upsilon_f}}z, \quad \tilde{\upsilon}_1 = r\Omega f'(\eta), \quad \tilde{\upsilon}_2 = r\Omega g(\eta), \\ &\tilde{\upsilon}_3 = -\sqrt{r\Omega\upsilon_f}f(\eta), \quad \beta(\eta) = \frac{T-T_\infty}{T_{ws}-T_\infty}, \\ &\gamma(\eta) = \frac{C-C_\infty}{C_{ws}-C_\infty}, \quad P = P_\infty+2\Omega\upsilon_f P(\eta) \end{aligned}\right\} \quad (8)$$

The system of non-linear ODEs obtained after the transformation are:

$$\frac{1}{T_1}f'''+ff''-\frac{1}{2}f'^2+\frac{1}{2}g^2-\frac{T_2}{T_1}\frac{M}{(1+m^2)}(f'-mg) - \frac{\lambda^*}{T_1}f'=0 \quad (9)$$

$$\frac{1}{T_1}g''+fg'-f'g-\frac{T_2}{T_1}\frac{M}{(1+m^2)}(g+mf')-\frac{\lambda^*}{T_1}g=0 \quad (10)$$

$$\frac{1}{P_r}\left(\frac{T_3}{T_4}+\frac{4}{3}N_{\text{rnd}}\right)\beta''+f\beta'+N_b\beta'\gamma'+N_t\beta'^2=0 \quad (11)$$

$$\gamma''+\frac{\text{Nt}}{\text{Nb}}\beta''+\text{Sc}f\gamma'=0 \quad (12)$$

The transformed limiting conditions are:

$$\left.\begin{aligned} &f'(0)=\vartheta f''(0), \quad f(0)=0, g(0)=1+\vartheta g'(0), \\ &\beta(0)=1+\alpha\beta'(0), \quad \gamma'(0)+\frac{N_t}{N_b}\beta'(0)=0, \quad \text{at } \eta=0, \\ &f'(\infty)\to 0, \quad g(\infty)\to 0, \quad \beta(\infty)\to 0, \\ &\gamma(\infty)\to 0 \quad \text{as } \eta\to\infty, \end{aligned}\right\} \quad (13)$$

From an engineering perspective, the parameter $C_{f_s}(\text{Re}_\alpha)^{1/2}$, $C_{g_s}(\text{Re}_\alpha)^{1/2}$ (representing skin friction), $N_{u_s}(\text{Re}_\alpha)^{-1/2}$ (the Nusselt number) and $S_{h_s}(\text{Re}_\alpha)^{-1/2}$ (the Sherwood number) are highly significant. These parameters are essential and described by the following non-dimensional equations:

$$C_{f_s}(\text{Re}_\alpha)^{1/2} = \frac{1}{T_1}f''(0), \quad C_{g_s}(\text{Re}_\alpha)^{1/2} = \frac{1}{T_1}g'(0),$$
$$N_{u_s}(\text{Re}_\alpha)^{-1/2} = -T_4\beta'(0), \quad N_{u_s}(\text{Re}_\alpha)^{-1/2} = -\gamma'(0)$$

Where;

$$\text{Re}_\alpha = \frac{\Omega r^2}{\upsilon_f}, \quad T_1 = (1-\varphi)^{5/2}\left(1-\varphi+\varphi\left(\frac{\rho_s}{\rho_f}\right)\right),$$
$$T_2 = (1-\varphi)^{5/2}\left(1-\varphi+\varphi\left(\frac{\sigma_s}{\sigma_f}\right)\right),$$

$$T_3=\frac{k_{\rm hnf}}{k_f},\quad T_4=(1-\varphi)^{5/2}\left(1-\varphi+\varphi\left(\frac{(\rho C_p)_s}{(\rho C_p)_f}\right)\right),$$

$$M=\frac{\sigma_f B_0^2}{2\rho_f\Omega},\ P_r=\frac{\upsilon_f}{(\rho C_p)_f},$$

$$\mathrm{Sc}=\frac{\upsilon_f}{D_B},\quad N_b=\frac{\tau D_B C_\infty}{\upsilon_f},\quad N_t=\frac{\tau D_T(T_{ws}-T_\infty)}{\upsilon_f T_\infty},$$

$$\vartheta=L^*{}_1\sqrt{\frac{2\Omega}{\upsilon_f}},\quad \alpha=L^*{}_2\sqrt{\frac{2\Omega}{\upsilon_f}},\quad N_{\rm rnd}=\frac{4\sigma^* T_\infty^3}{k^* k_f}$$

Here, M represent the magnetic field parameter, Pr denote the Prandtl number, Sc refers the Schmidt number, The parameters N_b and N_t relate to the influence of thermophoretic forces and Brownian particle movement, respectively, while ϑ is the velocity slip coefficient and α represent the thermal slip coefficient.

3. OVERLAPPING GRID SPECTRAL QUASILINEARIZATION SOLUTION

This iterative approach breaks the solution area into multiple intersecting sub-domain and employs quasi-linearization, an adapted Chebyshev spectral collocation approach alongside Lagrange interpolation using Gauss–Lobatto points. The Spectral Quasi-Linearization Method (SQLM) is recognized for its superior stability, accuracy, and reduced computational time compared to conventional computational approaches like the Runge–Kutta method, Shooting approach, and Keller–Box scheme are commonly employed. The application of SQLM greatly increases the precision and processing performance when used on multiple grids. This method demonstrates notable advantages, especially in maintaining stability across bigger sub-domains using fewer grid points, enhancing accuracy, and lowering computational cost. These improvements stem from the use of matrices of irregular coefficients, which streamline matrix-vector and inversion of the matrix operations, leading to faster computations. The implementation procedure is outlined below:

The nonlinear ODEs are transformed into a linear form through the quasilinearization method, following the conventional SQLM procedure., leading to

$$a^*{}_{0,r}f_r'''+a^*{}_{1,r}f_r''+a^*{}_{2,r}f_r'+a^*{}_{3,r}f_r+a^*{}_{4,r}g_r=R^*{}_{1,r}\tag{14}$$

$$b^*{}_{0,r}g_r''+b^*{}_{1,r}g_r'+b^*{}_{2,r}g_r+b^*{}_{3,r}f_r'+b^*{}_{4,r}f_r=R^*{}_{2,r}\tag{15}$$

$$c^*{}_{0,r}\beta_r''+c^*{}_{1,r}\beta_r'+c^*{}_{2,r}f_r+c^*{}_{3,r}\gamma_r'=R^*{}_{3,r}\tag{16}$$

$$d^*{}_{0,r}\gamma_r''+d^*{}_{1,r}\varphi_r'+d^*{}_{2,r}f_r+d^*{}_{3,r}\beta_r''=R^*{}_{4,r}\tag{17}$$

The variable coefficients are obtained with respect to the operators $(F,\ G,\ T,\ H)$ as:

$$\left.\begin{aligned}
&a^*{}_{0,r}=\frac{\partial F}{\partial f'''}=\frac{1}{T_1},\quad a^*{}_{1,r}=\frac{\partial F}{\partial f''}=f_r,\\
&a^*{}_{2,r}=\frac{\partial F}{\partial f'}=-f_r-\frac{T_2}{T_1}\left(\frac{M}{(1+m^2)}\right)-\frac{\lambda^*}{T_1},\\
&a^*{}_{3,r}=\frac{\partial F}{\partial f}=f_r{}'',\quad a^*{}_{4,r}=\frac{\partial F}{\partial g}=g_r-\frac{T_2}{T_1}\left(\frac{M}{(1+m^2)}\right)m,\\
&b^*{}_{0,r}=\frac{\partial G}{\partial g''}=\frac{1}{T_1},\quad b^*{}_{1,r}=\frac{\partial G}{\partial g'}=f_r,\\
&b^*{}_{2,r}=\frac{\partial G}{\partial g}=-f_r{}'-\frac{T_2}{T_1}\left(\frac{M}{(1+m^2)}\right)-\frac{\lambda^*}{T_1},\\
&b^*{}_{3,r}=\frac{\partial G}{\partial f'}=f_r{}'-\frac{T_2}{T_1}\left(\frac{M}{(1+m^2)}\right)m,\\
&b^*{}_{4,r}=\frac{\partial G}{\partial f}=g_r{}',\quad c^*{}_{0,r}=\frac{\partial T}{\partial \beta''}=\frac{1}{P_r}\left(\frac{T_3}{T_4}+\frac{4}{3}N_{\rm rnd}\right),\\
&c^*{}_{1,r}=\frac{\partial T}{\partial \beta'}=f_r+2N_t\beta_r'+N_b\gamma_r'\\
&c^*_{2,r}=\frac{\partial T}{\partial f}=\beta_r',\quad c^*_{3,r}=\frac{\partial T}{\partial \gamma'}=N_b\beta_r',\\
&d^*_{0,r}=\frac{\partial H}{\partial \gamma''}=1,\quad d^*_{1,r}=\frac{\partial H}{\partial \gamma'}=\mathrm{Sc}\,f_r,\\
&d^*_{2,r}=\frac{\partial H}{\partial f}=\mathrm{Sc}\gamma_r',\quad d^*_{3,r}=\frac{\partial H}{\partial \beta''}=\frac{N_t}{N_b},\\
&R^*{}_{1,r}=f_rf_r''-\frac{1}{2}f_r{}'^2+\frac{1}{2}g_r{}^2,\\
&R^*{}_{2,r}=f_rg_r'-f'{}_rg_r,\\
&R^*{}_{3,r}=f_r\beta_r'+N_t\beta_r'{}^2+N_b\beta_r'\gamma_r',\\
&R^*{}_{4,r}=\mathrm{Sc}\,f_r\gamma_r'
\end{aligned}\right\}\tag{18}$$

To illustrate the effectiveness regarding the breakdown of the conflicting domain SQLM, we begin by approximating the primary semi-infinite solution domain $(0,\ \infty)$ with a finite solution domain $I=[0,\ \eta_\infty]$. The selected η_∞ is sufficiently large enough to ensure that the flow characteristics closely approximate those at infinity.[35] The confined solution area I, is split into q overlapping computational regions, as illustrated below:

$$I_l=\left[\eta^l{}_0,\ \eta^l{}_{M_\eta}\right],\quad l=1,\ 2,\ 3,\ 4,\ \ldots\ldots,\ q\tag{19}$$

ARTICLE

Each subdomain, I_l is segmented into $M_\eta + 1$ collocation points with uniform domain length defined as:[36, 37]

$$L = \frac{\eta_\infty}{q + (1-q)\left(1 - \cos\left(\frac{\pi}{M_\eta}\right)\right)} \tag{20}$$

The total domain length is determined using the Gauss-Lobatto collocation points, $z_i = \cos\left(\pi\, i/M_\eta\right)$, $i = 0,\ 1,\ 2,\ 3,\ \ldots,\ M_\eta$ resulting in:

$$\eta = \frac{L}{2}\left(1 - \cos\left(\frac{\pi}{M_\eta}\right)\right)(1-q) + qL \tag{21}$$

We take into account how each interval is transformed, $I_l = [\eta^l{}_0,\ \eta^l{}_{M_\eta}]$ into $z_i = [-1,\ 1]$ by the use of the linear transformation $\eta^l{}_i = L/2\,(z_i + 1)$, $z_i = \cos\left(\pi i/M_\eta\right)$.

The unknown functions $f(\eta)$, $g(\eta)$, $\beta(\eta)$, and $\gamma(\eta)$ are each approximated using the univariate Langrange interpolation polynomial. The approximation of $f(\eta)$ for instance is defined as:

$$f(\eta) \approx F(\eta) = \sum_{i=0}^{M_\eta} F(\eta_i)\, V_i(\eta) \tag{22}$$

The functions $Vi(\eta)$ denote the Lagrange basis polynomials, with their respective derivatives approximated at the collocation nodes over the truncated interval.$\tilde{\eta}_j$ $(j = 0,\ 1,\ 2,\ \ldots\ldots,\ M_\eta)$ as:

$$\frac{df(\eta)}{d\eta} \approx \sum_{i=0}^{M_\eta} F(\eta_i)\, V'_i(\eta) = \sum_{i=0}^{M_\eta} \boldsymbol{D}^l{}_{i,j} \boldsymbol{F}^l(\eta_j) = \boldsymbol{D}^l \boldsymbol{F} \tag{23}$$

Where $\boldsymbol{D}^l = 2/(\eta^l{}_{M_\eta} - \eta^l{}_0)\,\bar{D}$ is the differential matrix on I_l and $\boldsymbol{F} = [f(\eta^l{}_0),\ f(\eta^l{}_1),\ \ldots\ldots,\ f(\eta^l{}_{M_\eta})]^T$. $\bar{D}$ represents the basic the Chebyshev differential matrix which is a differential operator of the first order with order $(M_\eta + 1) \times (M_\eta + 1)$. An approximation of the n-nth-order derivative of f wrt space over the full domain is given by:

$$\frac{d^n f}{d\eta^n} \approx \boldsymbol{D}^n \hat{\boldsymbol{F}} \tag{24}$$

The newly defined matrix-vector $\widehat{\boldsymbol{F}}$, representing the solution over the entire set of sub-intervals, can be expressed as follows:

$$\hat{\boldsymbol{F}} = \left[f(\eta_c),\ f(\eta_1),\ \ldots,\ f\left(\eta_{M_\eta}\right)\right]^T \tag{25}$$

A comparable approach is employed to provide a close representation of the other unknown functions and their respective derivatives. Once the spectral collocation technique has been applied, the discrete derivatives on (9)–(12), the resulting matrix equations are as follows

$$\boldsymbol{A}_{1,1}\hat{\boldsymbol{F}} + \boldsymbol{A}_{1,2}\hat{\boldsymbol{G}} + \boldsymbol{A}_{1,3}\hat{\boldsymbol{T}} + \boldsymbol{A}_{1,4}\hat{\boldsymbol{H}} = \boldsymbol{R}_{1,r} \tag{26}$$

$$\boldsymbol{A}_{2,1}\hat{\boldsymbol{F}} + \boldsymbol{A}_{2,2}\hat{\boldsymbol{G}} + \boldsymbol{A}_{2,3}\hat{\boldsymbol{T}} + \boldsymbol{A}_{2,4}\hat{\boldsymbol{H}} = \boldsymbol{R}_{2,r} \tag{27}$$

$$\boldsymbol{A}_{3,1}\hat{\boldsymbol{F}} + \boldsymbol{A}_{3,2}\hat{\boldsymbol{G}} + \boldsymbol{A}_{3,3}\hat{\boldsymbol{T}} + \boldsymbol{A}_{3,4}\hat{\boldsymbol{H}} = \boldsymbol{R}_{3,r} \tag{28}$$

$$\boldsymbol{A}_{4,1}\hat{\boldsymbol{F}} + \boldsymbol{A}_{4,2}\hat{\boldsymbol{G}} + \boldsymbol{A}_{4,3}\hat{\boldsymbol{T}} + \boldsymbol{A}_{4,4}\hat{\boldsymbol{H}} = \boldsymbol{R}_{4,r} \tag{29}$$

Equations (26)–(29) can be expressed in matrix form as:

$$\begin{bmatrix} \boldsymbol{A}_{1,1} & \boldsymbol{A}_{1,2} & \boldsymbol{A}_{1,3} & \boldsymbol{A}_{1,4} \\ \boldsymbol{A}_{2,1} & \boldsymbol{A}_{2,2} & \boldsymbol{A}_{2,3} & \boldsymbol{A}_{2,4} \\ \boldsymbol{A}_{3,1} & \boldsymbol{A}_{3,2} & \boldsymbol{A}_{3,3} & \boldsymbol{A}_{3,4} \\ \boldsymbol{A}_{4,1} & \boldsymbol{A}_{4,2} & \boldsymbol{A}_{4,3} & \boldsymbol{A}_{4,4} \end{bmatrix} \begin{bmatrix} \hat{\boldsymbol{F}} \\ \hat{\boldsymbol{G}} \\ \hat{\boldsymbol{T}} \\ \hat{\boldsymbol{H}} \end{bmatrix} = \begin{bmatrix} \boldsymbol{R}_{1,r} \\ \boldsymbol{R}_{2,r} \\ \boldsymbol{R}_{3,r} \\ \boldsymbol{R}_{4,r} \end{bmatrix} \tag{30}$$

Where;

$$\boldsymbol{A}_{1,1} = \left[\boldsymbol{a}^*{}_{0,r}\boldsymbol{D}^3 + \boldsymbol{a}^*{}_{1,r}\boldsymbol{D}^2 + \boldsymbol{a}^*{}_{2,r}\boldsymbol{D} + \boldsymbol{a}^*{}_{3,r}\right],$$

$$\boldsymbol{A}_{1,2} = \left[\boldsymbol{a}^*{}_{4,r}\boldsymbol{D}\right],\quad \boldsymbol{A}_{1,3} = 0,\quad \boldsymbol{A}_{1,4} = 0,$$

$$\boldsymbol{A}_{2,1} = \left[\boldsymbol{b}^*{}_{3,r}\boldsymbol{D}^2 + \boldsymbol{b}^*{}_{4,r}\boldsymbol{D}\right],$$

$$\boldsymbol{A}_{2,2} = \left[\boldsymbol{b}^*{}_{0,r}\boldsymbol{D}^2 + \boldsymbol{b}^*{}_{1,r}\boldsymbol{D} + \boldsymbol{b}^*{}_{2,r}\right],$$

$$\boldsymbol{A}_{2,3} = 0,\quad \boldsymbol{A}_{2,4} = 0,$$

$$\boldsymbol{A}_{3,1} = \left[\boldsymbol{c}^*{}_{2,r}\right],\ \boldsymbol{A}_{3,2} = 0,\ \boldsymbol{A}_{3,3} = \left[\boldsymbol{c}^*{}_{0,r}\boldsymbol{D}^2 + \boldsymbol{c}^*{}_{1,r}\boldsymbol{D}\right],$$

$$\boldsymbol{A}_{3,4} = [\boldsymbol{c}^*{}_{3,r}\boldsymbol{D}],\quad \boldsymbol{A}_{4,1} = \left[\boldsymbol{d}^*{}_{2,r}\right],\ \boldsymbol{A}_{4,2} = 0,$$

$$\boldsymbol{A}_{4,3} = \left[\boldsymbol{d}^*{}_{0,r}\boldsymbol{D}^2\right],\quad \boldsymbol{A}_{4,4} = \left[\boldsymbol{d}^*{}_{0,r}\boldsymbol{D}^2 + \boldsymbol{d}^*{}_{1,r}\boldsymbol{D}\right]$$

A sparser matrix system is derived by applying the boundary conditions to the main diagonal sub-matrices within matrix system (30), the system is subsequently solved using appropriate initial estimates that comply with the boundary conditions, allowing for the simultaneous computation of numerical solutions across all subdomains. The initial guesses adopted for the present model are as follows:

$$\left.\begin{aligned} f_0(\eta) &= 0, \\ g_0(\eta) &= \left(\frac{1}{(1+\vartheta)}\right) e^{-\eta}, \\ \beta_0(\eta) &= \left(\frac{1}{(1+\alpha)}\right) e^{-\eta}, \\ \gamma_0(\eta) &= -\left(\frac{N_t}{N_b}\right) e^{-\eta} \end{aligned}\right\} \tag{31}$$

4. VALIDATION

Table II presents the numerically obtained results of $-\beta'(0)$ and compares them with the results from the previously published study.[32] The values computed using the overlapping grid SQLM show excellent agreement with the reference study, as shown in Table II, confirming the high accuracy, dependability and effectiveness of the suggested approach. To further evaluate the method's performance, convergence behavior was assessed by analyzing solution and residual errors. Solution errors were determined by comparing function values across successive iterations. Additionally, residual errors were computed by the infinity norm and replacing the approximate solutions into Eqs. (9–12) of the resulting discrepancies. Figures 2–5 illustrate the

Table II. Comparison of the numerical values of the Nusselt number against results of Mustafa[32] for different values of P_r, M and N_t.

P_r	M	N_t	Mustafa[32]	Present study
5.0	0.5	0.5	0.254657	0.25465673
6.2			0.276789	0.27678914
8.0			0.303769	0.30376926
13.0			0.358263	0.35826315
7.0	0		0.482752	0.48275174
	0.2		0.399324	0.39932407
	0.4		0.323281	0.32328124
	0.8		0.206541	0.20654127
	0.5	0.1	0.407715	0.40771454
		0.3	0.347439	0.34743863
		0.5	0.289524	0.28952413
		0.7	0.180515	0.18051547

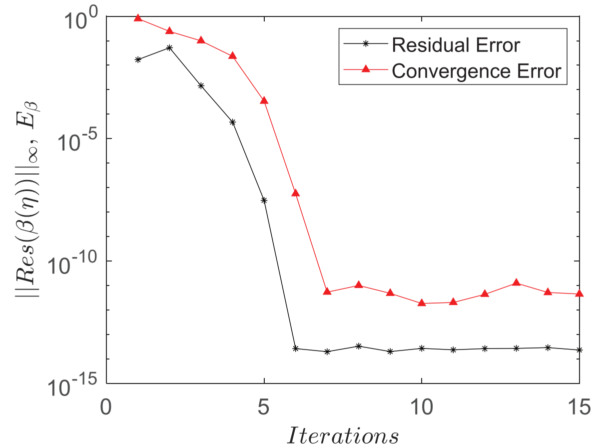

Fig. 4. Residual and convergence errors for $\beta(\eta)$.

error trends for $f(\eta)$, $g(\eta)$, $\beta(\eta)$ and $\gamma(\eta)$, respectively. Initially, convergence errors are relatively high due to the use of an approximate initial guess, which may be far from the true solution. However, these errors drop sharply—by several orders of magnitude—within the first five iterations, reaching approximately 10^{-13} for $f(\eta)$, $g(\eta)$, and 10^{-12} for $\beta(\eta)$, $\gamma(\eta)$. The rapid fall indicates that the procedure is quickly approaching a stable solution. This rapid decline indicates that the method converges quickly toward a stable solution. After the fifth iteration, the convergence error levels off, implying that further iterations result in negligible changes, thus confirming convergence. The trends observed in the residual errors closely mirror those of the convergence errors, starting at high values and decreasing significantly within the first few iterations. This suggests that the early stages of the procedure are effective at narrowing the gap between numerical and analytical solutions. The residual error approaches its minimum around the same number of iterations as the convergence error, indicating that the solution has stabilized. It's worth noting that the residual error for $f(\eta)$, $\beta(\eta)$, and $\gamma(\eta)$ reduces to approximately 10^{-14}, and for $g(\eta)$ it reaches around 10^{-17}, which is lower than the convergence error. This illustrates that the numerical method is quite precise in meeting the governing equations, even when small changes in the solution occur between iterations.

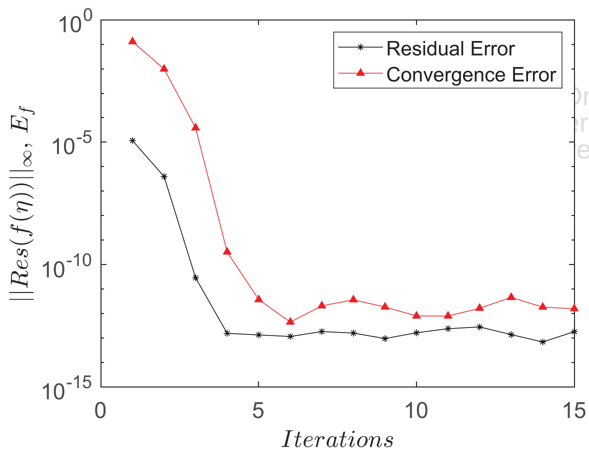

Fig. 2. Residual and convergence errors for $f(\eta)$.

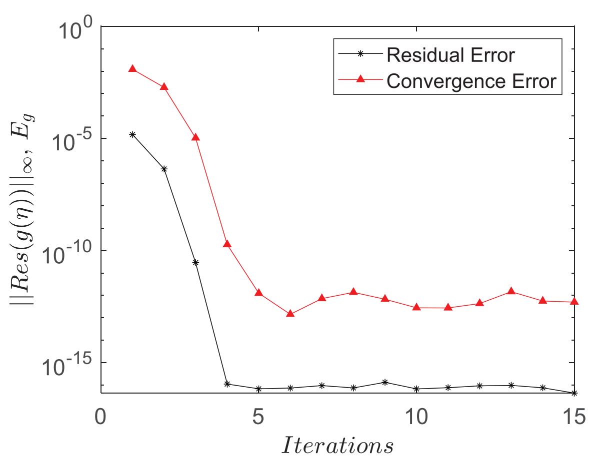

Fig. 3. Residual and convergence errors for $g(\eta)$.

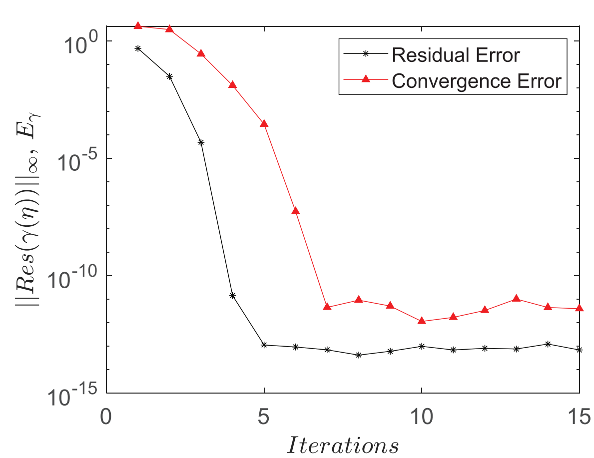

Fig. 5. Residual and convergence errors for $\gamma(\eta)$.

ARTICLE

Default values:

$$\left.\begin{array}{c} \lambda^* = 0.2, \quad M = 0.5, \quad \vartheta = 0.25, \\ P_r = 7.0, \quad N_b = 0.5, \quad N_t = 0.7, \\ w_f = w_1 = w_2 = 2.0, \quad n = 3.0, \quad \alpha = 0.25, \\ N_{\mathrm{rnd}} = 0.5, \quad \varphi_1 = 0.1, \quad \varphi_2 = 0.2, \end{array}\right\}$$

5. RESULTS AND DISCUSSION

This segment provides a comprehensive and in-depth examination of the temperature, concentration, and characteristics of the conducting hybrid nanofluid's movement made of carbon nano tubes (CNTs) and iron oxide (Fe_3O_4) above a revolving disc. The model is based on several key assumptions, including steady-state flow in an impermeable substance, the impact of a consistent magnetic field, the consideration of Hall currents, Buongiorno contribution, temperature leap and sliding velocity, all of which introduced different parameters to the model. The influence of some of these variables are presented with tables and figures, as well as a detailed analysis of the distributions of temperature, velocity, and concentration. Furthermore, the Sherwood, Nusselt, and skin friction numbers are displayed.

The application of a magnetic field introduces electromagnetic interactions that influence the motion of nanoparticles suspended in the fluid. The resulting Lorentz force acts in a direction perpendicular to both the magnetic field lines and the velocity of the fluid, thereby opposing and slowing the fluid's motion. Figure 6 for axial velocity $f(\eta)$, Figure 7 for radial velocity $f'(\eta)$, and Figure 8 for tangential velocity $g(\eta)$ show a significant decrease in fluid velocity across all components as the magnetic parameter M increases. In Figure 9, we observed that axial velocity decreases as the porosity parameter increases. This is because a higher porosity means a less permeable medium, which increases fluid resistance by forcing the fluid to flow via narrower channels. The centrifugal

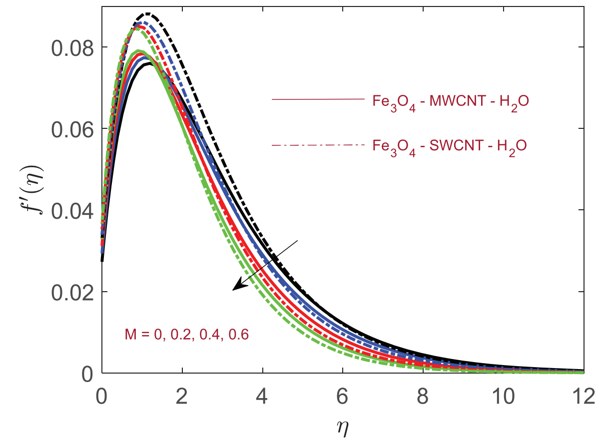

Fig. 7. The influence of M on $f'(\eta)$.

force generated by the disk's spinning principally drives the fluid's radial motion. In a porous medium, raising the porosity parameter increases the effective drag force in the radial direction, reducing radial velocity, as seen in Figure 10. The peak of radial velocity occurs close to the rotating disk. In Figure 12, with a rise in porosity value, the tangential velocity decreases. This reduction is most noticeable close to the surface of the disk. Hall current generally causes deflection of charged particles within a conducting fluid, affecting the overall current density distribution within the fluid and lessening the impact of the Lorentz force on the fluid motion. As the Hall current parameter m increases, the opposition to fluid flow decreases, resulting in an acceleration of the fluid, which explains the increase in the velocity profiles in all directions as depicted by Figures 13–15. The velocity slip condition minimizes the fluid's interaction with the surface, resulting in a smaller boundary layer.

Figures 15–17 show that the thinning effect reduces velocity near the surface by transferring less momentum into the fluid. In general, from Figures 6–17, the MWCNT$-Fe_3O_4-H_2O$ hybrid nanofluid significantly out-

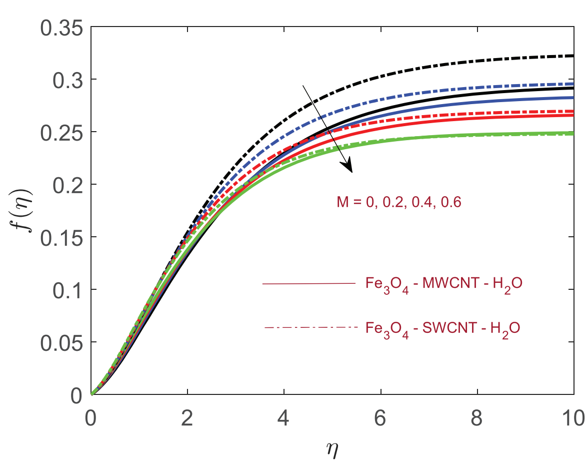

Fig. 6. The influence of M on $f(\eta)$.

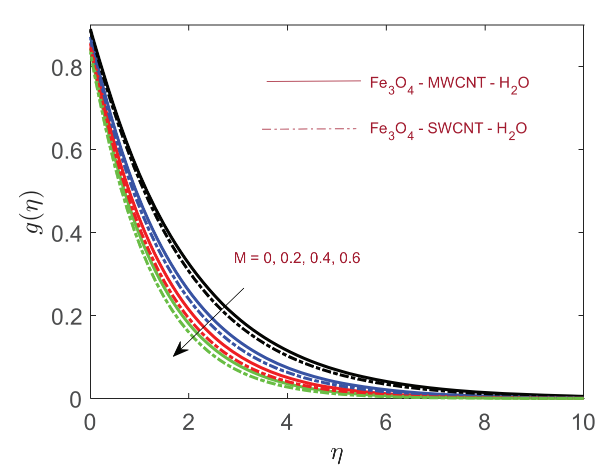

Fig. 8. The influence of M on $g(\eta)$.

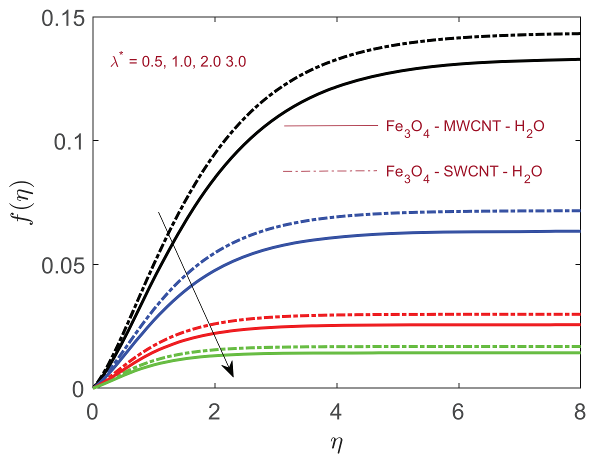

Fig. 9. The influence of λ^* on $f(\eta)$.

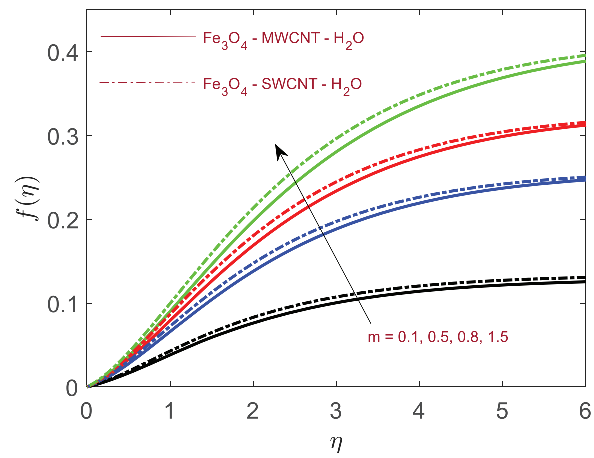

Fig. 12. The influence of m on $f(\eta)$.

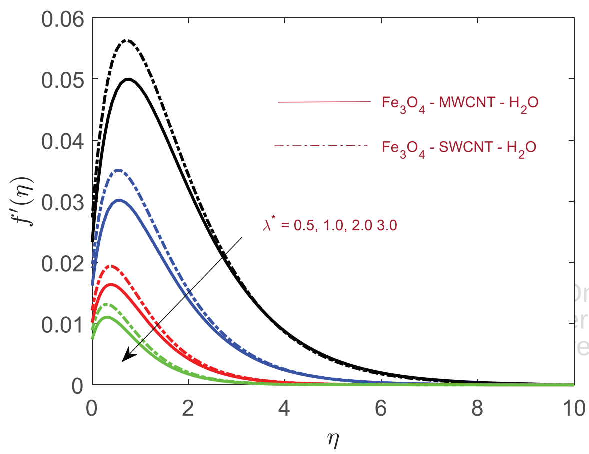

Fig. 10. The influence of λ^* on $f'(\eta)$.

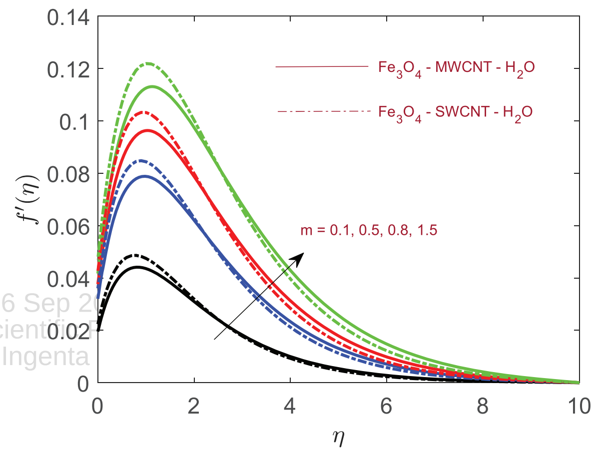

Fig. 13. The influence of m on $f'(\eta)$.

performs the SWCNT$-Fe_3O_4-H_2O$ in terms of the velocity distributions owing to the presence of nanoparticles of larger diameter and multiple graphene layers in the structure of MWCNT.

In Figure 18 we identified that the temperature distribution of both MWCNT$-Fe_3O_4-H_2O$ and SWCNT$-Fe_3O_4-H_2O$ Rises as the parameter value grows of the magnetic parameter M. Physically, the increase in temperature distribution with increasing M

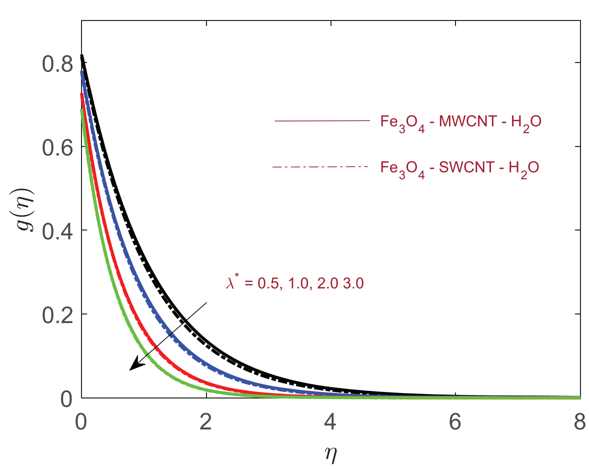

Fig. 11. The influence of λ^* on $g(\eta)$.

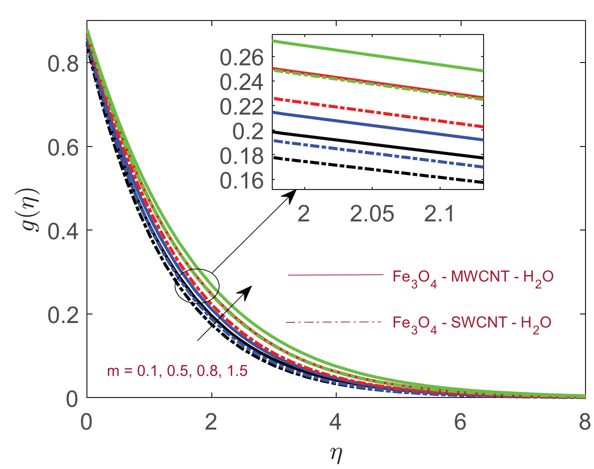

Fig. 14. The influence of m on $g(\eta)$.

ARTICLE

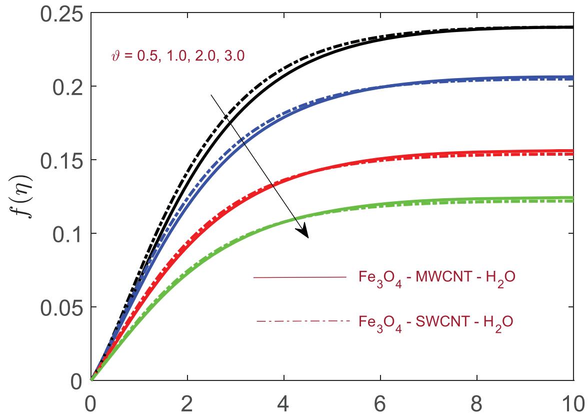

Fig. 15. The influence of ϑ on $f(\eta)$.

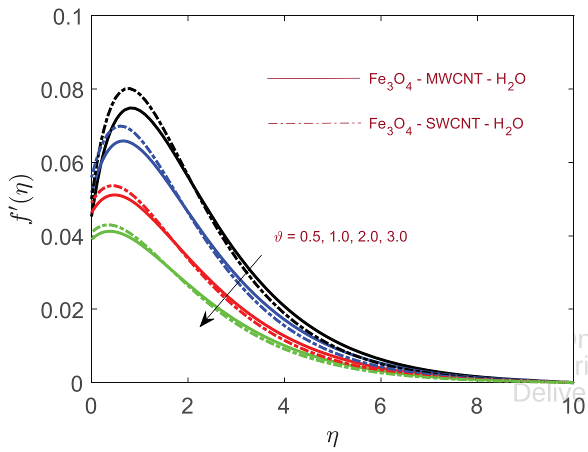

Fig. 16. The influence of ϑ on $f'(\eta)$.

is largely driven by electromagnetic effects, specifically the enhanced Joule heating and the restriction of heat convection mechanisms due to the Lorentz force, which facilitate the more local heat retention and conversion of mechanical energy to heat energy. Figure 19 displays the thermal profile of the nanofluid as the Prandtl number

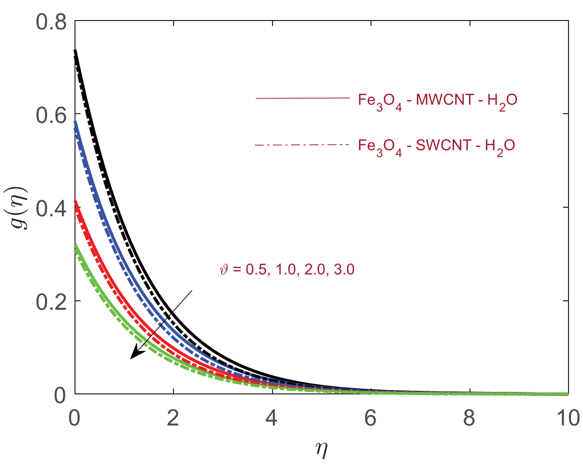

Fig. 17. The influence n of ϑ on $g(\eta)$.

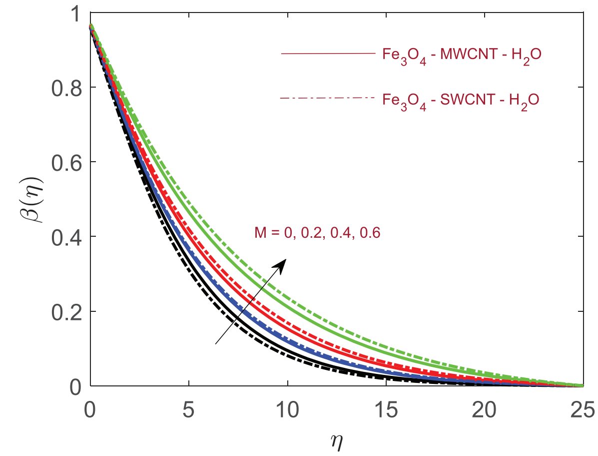

Fig. 18. Repercussion of M on $\beta(\eta)$.

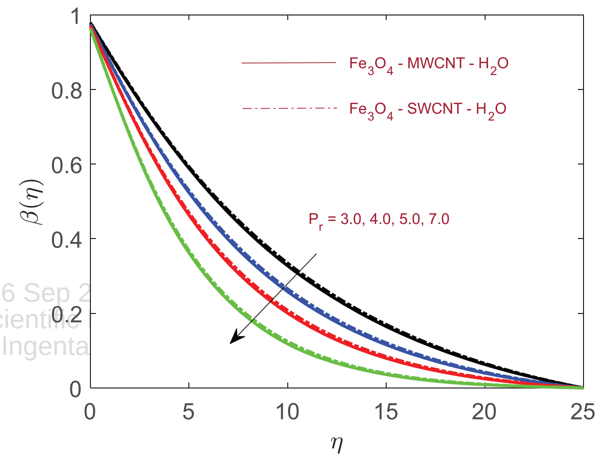

Fig. 19. Repercussion of P_r on $\beta(\eta)$.

is elevated in values. As seen, the temperature distribution of the fluid improves with higher P_r. It can also be observed that for any particular P_r value, the temperature distribution of MWCNT$-Fe_3O_4-H_2O$ is slightly higher

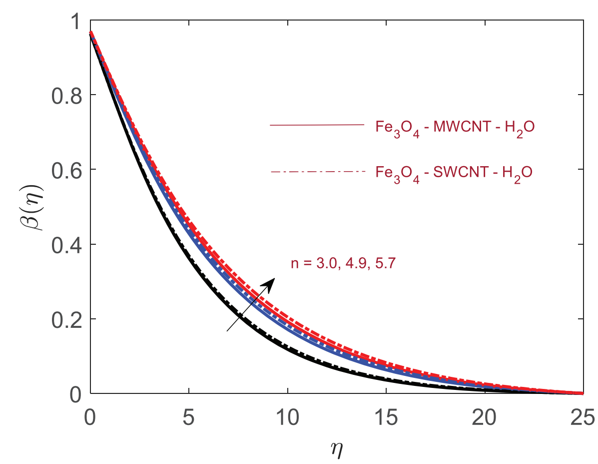

Fig. 20. Repercussion of n on $\beta(\eta)$.

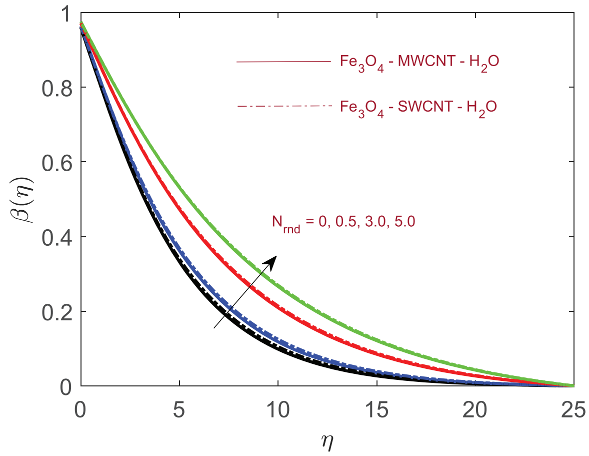

Fig. 21. Repercussion of $N_{\rm rnd}$ on $\beta(\eta)$.

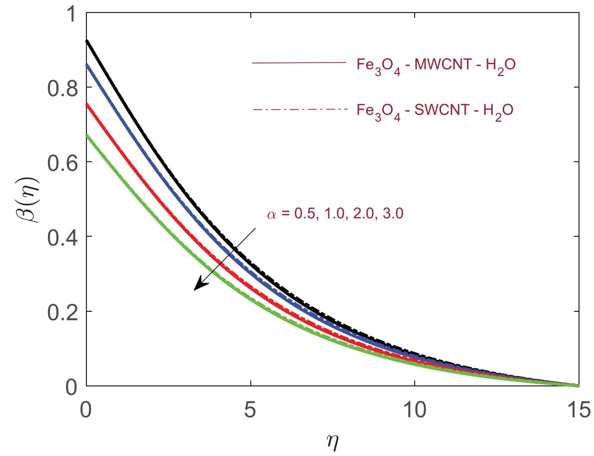

Fig. 24. The influence of α on $\beta(\eta)$.

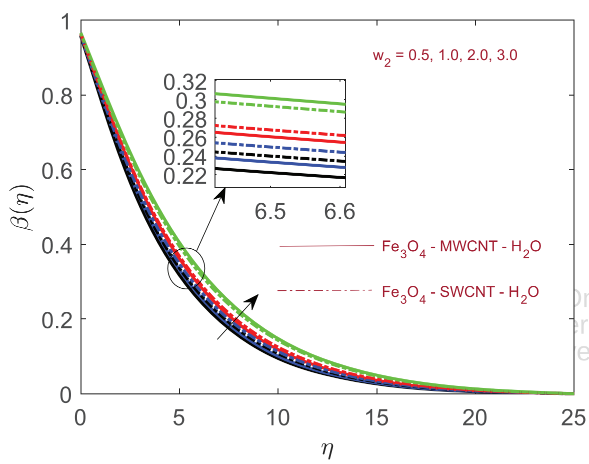

Fig. 22. The influence of w_2 on $\beta(\eta)$.

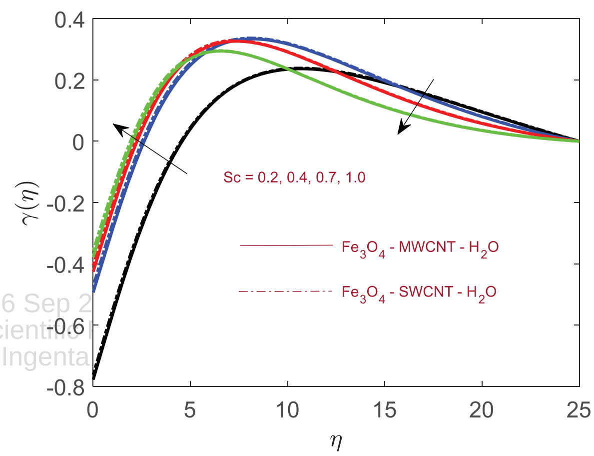

Fig. 25. The influence of Sc on $\gamma(\eta)$.

than that of SWCNT$-Fe_3O_4-H_2O$ highlighting the better thermal conductivity offered by MWCNT. Generally, the shapes of the nanoparticles greatly influence the thermal distribution of the fluid, owing to the interactions between the nanoparticles and the surrounding fluid. These interactions depend largely on the surface area-to-volume ratio of the nanoparticles. As the surface area to volume ratio increases, the interactions become more rigorous, resulting in a uniform and higher fluid temper-

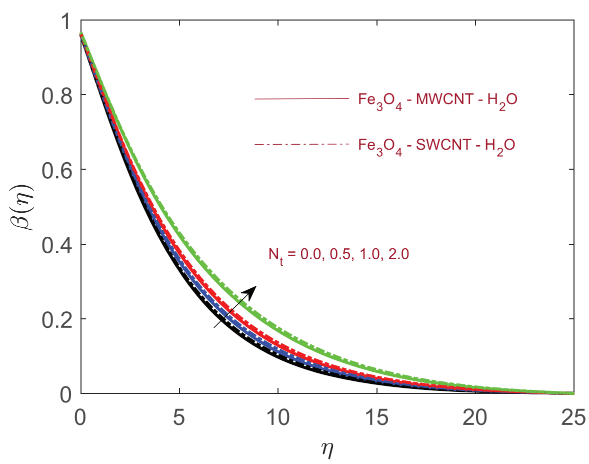

Fig. 23. The influence of N_t on $\beta(\eta)$.

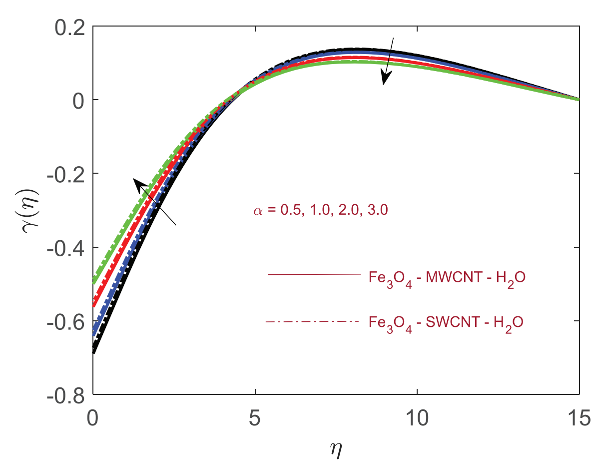

Fig. 26. The influence of α on $\gamma(\eta)$.

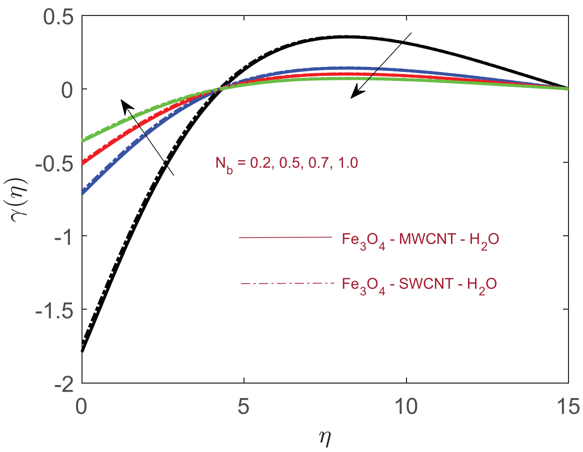

Fig. 27. The influence of N_b on $\gamma(\eta)$.

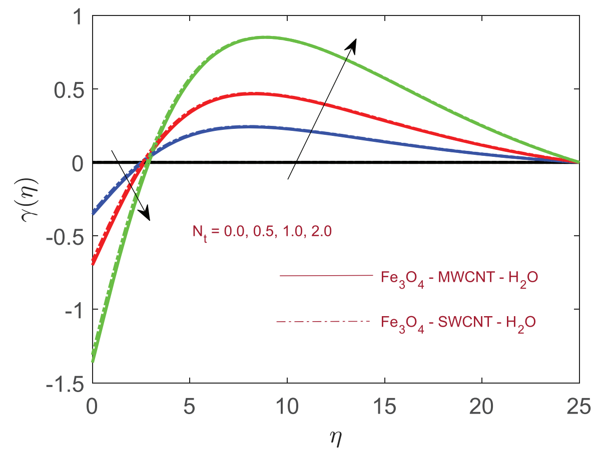

Fig. 30. The influence of N_t on $\gamma(\eta)$.

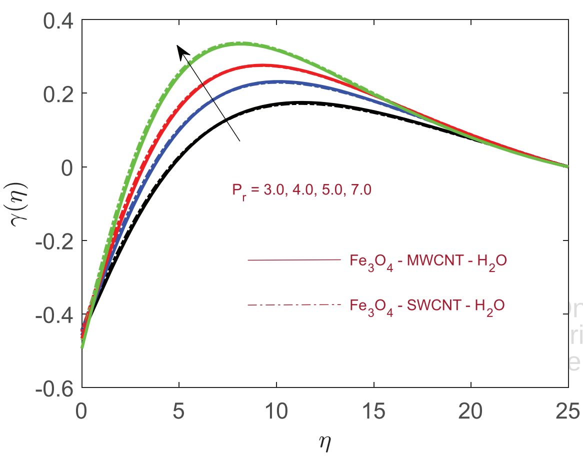

Fig. 28. The influence of P_r on $\gamma(\eta)$.

ature distribution. This key concept is demonstrated in Figure 20, which presents the response of the thermal profile to changes in the shape of the Fe_3O_4 nanoparticles with $n = 3$ (spherical shape) offering the least surface to volume ratio and $n = 5.7$ (platelet shape) the highest surface to volume ratio for both hybrid nanofluid compositions. Figure 21 displays an increasing trend in the thermal profile as the thermal radiation parameter N_{rnd} increases for both cases of the hybrid nanofluid. Physically, increasing N_{rnd} means that thermal radiation becomes more significant in the energy balance of the system. The hybrid nanofluid absorbs the excess thermal radiation, which increases the energy within and, hence, a significant elevation of the temperature profile of the fluid. In Figure 22, we observed an elevated temperature movement of the fluid as the Carbon nanotubes' mass-fraction increased. Carbon nanotubes have extremely high thermal conductivity, particularly MWCNT and SWCNT, As their concentration increases in the hybrid nanofluid, the fluid's overall conductivity of heat rises. This improvement makes it possible for the fluid to transmit heat more efficiently through its volume. Similar trends are observed for different values of the thermophoresis parameter in Figure 23. Figure 24 shows how the blended nanofluid temperature distribution is affected by the thermal slip parameter α. Typically, in the absence of thermal slip ($\alpha = 0$) for this configuration, the fluid adjacent to the disk would assume

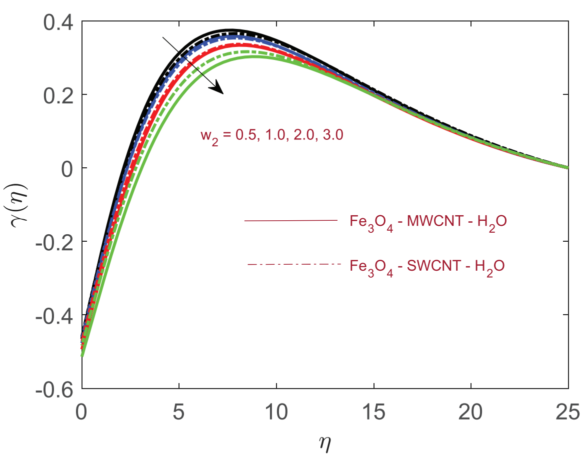

Fig. 29. The influence of w_2 on $\gamma(\eta)$.

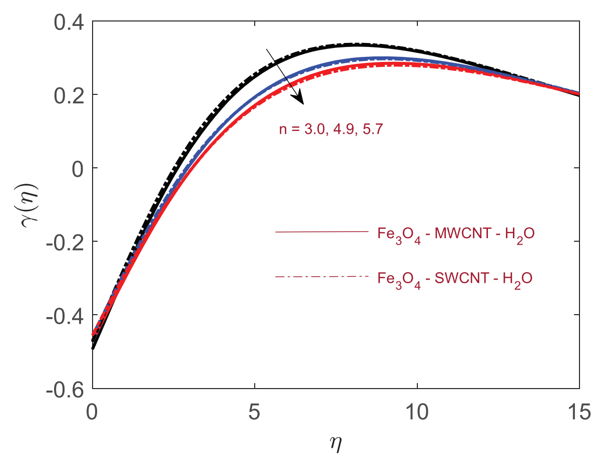

Fig. 31. The influence of n on $\gamma(\eta)$.

ARTICLE

Table III. Values of skin friction coefficients in numbers $(\mathrm{Re}_\alpha)^{1/2}C_{f_s}$ and $(\mathrm{Re}_\alpha)^{1/2}C_{g_s}$ for different values of M, m, λ^*, ϑ and w_2.

M	m	λ^*	ϑ	w_2	$(\mathrm{Re}_\alpha)^{1/2}C_{f_s}$ – MWCNT	$(\mathrm{Re}_\alpha)^{1/2}C_{f_s}$ – SWCNT	$(\mathrm{Re}_\alpha)^{1/2}C_{g_s}$ – MWCNT	$(\mathrm{Re}_\alpha)^{1/2}C_{g_s}$ – SWCNT
0.0	0.5	0.2	0.25	2.0	0.24051154	0.22886179	− 0.96394971	−0.79254224
0.5					0.28256876	0.25256085	− 1.32777183	− 1.10999031
1.0					0.31440325	0.27404697	− 1.58302705	− 1.32922879
2.0					0.35917301	0.30578598	− 1.95310137	− 1.64306979
0.5	0.0				0.14044403	0.12940168	−1.34959800	−1.12458576
	0.5				0.28256876	0.25256085	−1.32777183	−1.10999031
	1.0				0.35083879	0.31341483	−1.24940632	−1.04509370
	2.0				0.36500946	0.32954821	−1.13178288	−0.99196393
	0.5	0.1			0.32295162	0.28393216	−1.22296580	−1.03510357
		0.5			0.20582993	0.18932635	−1.59697314	−1.30746466
		1.0			0.14293673	0.13403548	−1.93771796	−1.56531512
		2.0			0.08968427	0.08515772	−2.40916927	−1.93000964
		0.2	0.0		0.42641747	0.39090745	−1.54618670	−1.30150327
			0.5		0.19968830	0.17536128	−1.15694486	−0.96079017
			1.0		0.11409110	−0.91627605	0.09801935	−0.75350621
			2.0		0.05106475	−0.64569923	0.04295476	−0.52526850
			0.25	0.0	0.19865521	−0.83497916	0.19865521	−0.83497916
				0.5	0.21781581	−0.92450130	0.21164859	− 0.89034989
				1.0	0.23889693	−1.03704079	0.22526162	− 0.95552334
				3.0	0.32369303	− 1.70966357	0.27834498	− 1.29356051

a temperature very close to that of the disk, resulting in a strong thermal boundary layer. However, as the slip increases, thermal contact reduces, resulting in less energy being transferred to the fluid and, thus, a lower temperature profile near the surface. This temperature reduction within the boundary layer indicates a less effective heat transfer process, which is significant in applications requiring thermal management and temperature gradient control.

Figure 25 depicts dynamic characteristics of the hybrid nanofluid concentration as Schmidt number, Sc increases. With a higher Sc, the mass diffusivity decreases, meaning that the ability of the nanoparticles to diffuse away from the disk is reduced. As a result, the nanoparticles tend to accumulate near the disk surface, leading to a higher concentration in this region. The rotating motion of the disk creates a strong centrifugal force, pushing

Table IV. Numerical values of Nusselt number $(\mathrm{Re}_\alpha)^{-1/2}N_{u_s}$ for different values of M, a, w_2, P_r, N_t and N_{rnd}.

M	α	w_2	P_r	N_t	N_{rnd}	$(\mathrm{Re}_\alpha)^{-1/2}N_{u_s}$ – MWCNT	$(\mathrm{Re}_\alpha)^{-1/2}N_{u_s}$ – SWCNT
0.0	0.25	0.5	7.0	0.7	0.5	0.76078542	0.84520727
0.5						0.75179019	0.80330111
1.0						0.73112091	0.76968758
2.0						0.69318650	0.72135326
0.5	0.2					0.75791502	0.80985005
	0.4					0.73397266	0.78424985
	0.7					0.70066963	0.74864103
	1.0					0.67016300	0.71602266
	0.25	0.0				0.83739200	0.86905562
		0.5				0.82108886	0.85519569
		1.0				0.80064775	0.83918586
		2.0				0.69947790	0.76548204
		0.5	5.0			0.66047226	0.70510977
			6.0			0.70626036	0.75429699
			7.0			0.75179019	0.80330111
			8.0			0.79687279	0.85191684
			7.0	0.2		0.77254944	0.82583520
				0.7		0.75179019	0.80330111
				1.0		0.73940776	0.78987687
				2.0		0.69869384	0.74582801
				0.7	0.0	0.78293776	0.83550387
					0.5	0.75179019	0.80330111
					3.0	0.65281091	0.69968612
					5.0	0.60885840	0.65301516

Table V. Numerical values of Sherwood number $(\mathrm{Re}_\alpha)^{-1/2}S_{h_s}$ for different values of M, a, w_2, P_r, N_t and N_{rnd}.

M	α	w_2	P_r	N_t	N_b	$(\mathrm{Re}_\alpha)^{-1/2}S_{h_s}$ − MWCNT	$(\mathrm{Re}_\alpha)^{-1/2}S_{h_s}$ − SWCNT
0.0	0.25	0.5	7.0	0.7	0.5	−0.23804758	−0.24801818
0.5						−0.23541866	−0.23572121
1.0						−0.22894620	−0.22585763
2.0						−0.21706726	−0.21167438
0.5	0.2					−0.23733662	−0.23764293
	0.4					−0.22733662	−0.23013079
	0.7					−0.21941056	−0.21968172
	1.0					−0.20985759	−0.21011016
	0.25	0.0				−0.26222436	−0.25501625
		0.5				−0.25711913	−0.25094919
		1.0				−0.25071812	−0.24625125
		2.0				−0.21903738	−0.22462355
		0.5	5.0			−0.20682299	−0.20690787
			6.0			−0.22116126	−0.22134140
			7.0			−0.23541866	−0.23572121
			8.0			−0.24953601	−0.24998704
			7.0	0.2		−0.06911980	−0.06923818
				0.7		−0.23541866	−0.23572121
				1.0		−0.33077311	−0.33111712
				2.0		−0.62511958	−0.62530360
				0.7	0.	−0.58854665	−0.58930302
					0.	2 −0.16815619	−0.16837229
					1.0	−0.11770933	−0.11786060
					2.0	−0.05885467	−0.05893030

the nanoparticles outward. However, with low mass diffusivity, they can disperse into the fluid away from the disk less. Away from the disk, the mass flux decreases significantly. Similar trends are evident in the concentration profile of increasing values of the thermal slip and Brownian motion parameters, as seen in Figures 26 and 27. Increasing Prandtl number significantly elevates the fluid mass flux for both $MWCNT-Fe_3O_4-H_2O$ and $SWCNT-Fe_3O_4-H_2O$ as depicted in Figure 28. Reverse trends are observed in Figure 29 as the mass-fraction of Fe_3O_4 increases owing to the existence of larger and heavier nanoparticles. Figure 30 showcases the hybrid nanofluid mass flux characteristics in response to variation of the thermophoresis parameter. It can be observed that close to the rotating disk, where the temperature is typically higher due to friction and heat generation, thermophoresis causes nanoparticles to depart from the disk surface. As N_t increases, the strength of this migration increases, leading to a more significant depletion of nanoparticles near the disk surface. As the nanoparticles move away from the disk surface, they accumulate in regions with less steep temperature gradients and weaker thermophoretic force. Figure 31 displays the influence of the shape factor of Fe_3O_4 nanoparticles with the concentration decreasing as the shapes change from spherical to cylindrical and finally to platelet.

Table III presents the computational values of the radial stress and defying torque at the rotating disk surface for varying values of M, m, λ^*, ϑ, and w_2 Increasing values of M, m, and w_2 increase the surface radial stress owing to the increase in the opposing forces as a result of the magnetic force interaction with the fluid, influence of the Hall current and mass-fraction of the (Fe_3O_4) nanoparticles with the variations more pronounced in MWCNT than SWCNT. Radial stress decreases with rising values of the porosity λ^* and slip ϑ parameters. The trends observed in the surface resisting torque are in reversed directions to those of radial stress.

1. Table IV displays the computed values of the heat transfer rate at the disk surface for different values of M, α, w_2, P_r, N_t, and N_{rnd}. In general, heat transfer rate is a critical undefined quantity that characterizes the rate of heat transfer in a fluid flow. It represents the Comparison between convective and conductive heat flux at the boundary surface. It is used to assess heat transfer efficiency in systems involving fluid flow. The hybrid fluid temperature is significantly reduced for increasing values of the M, w_2, α, N_t, and N_{rnd}. When M increases, the induced Lorentz force generates an opposing effect on the fluid motion, which usually results in a decrease in fluid velocity. This diminution of mobility reduces the transfer of heat through convection within the boundary layer. In a similar version, increasing N_t leads to a thickening of the thermal boundary layer as the nanoparticles, which have high thermal conductivity, move deeper into the fluid. This thickened boundary layer reduces the temperature gradient at the wall, resulting in a lower Nusselt number. Similar trends are observed for increasing values of the mass-fraction of the Fe_3O_4 nanoparticles, temperature slip and thermal radiation parameters. An increase in the Prandtl

number enhances the heat transfer rate, primarily because higher values lead to reduced thermal diffusivity, resulting in a thinner thermal boundary layer compared to the momentum boundary layer.

Table V serves the purpose of showcasing how the surface mass flux rate changes in response to variations in N_b, M, α, w_2, P_r, and N_t. Increasing the Brownian motion parameter improves the diffusion of nanoparticles, which subsequently influences the concentration gradients within the fluid. As such, the erratic motion of the particles intensifies, and the overall mass transfer rate is enhanced. Increase in the thermal slip parameter is accompanied by reduction in boundary layer thickness which forces a stronger convective response to maintain the nanoparticle concentration gradient, hence, increases the Sherwood number. Similar observations are made for the mass-fraction of (Fe_3O_4) nanoparticles and magnetic parameters. Increasing N_t weakens the concentration gradient which is a major factor that drives the mass flux close to the revolving disc. The reduction in the concentration gradient near the surface due to increased thermophoretic movement causes the process of transferred mass to drop. This also holds true for rising Prandtl number levels.

6. CONCLUSION

This study presents a comprehensive investigation into the flow, temperature, and concentration characteristics of a hybrid nanofluid composed of carbon nanotubes (CNTs) and iron oxide (Fe_3O_4) over a rotating disk. The study considers a range of physical factors such as magnetic field, Hall current, and slip conditions. The analysis, conducted through numerical simulations with an overlapping spectral quasilinearization method, ensures high accuracy and convergence. The significant findings of this research, particularly in practical application areas such as enhanced lubricant production, spacecraft thermal control systems, enhanced oil recovery (EOR), and electronics thermal management, can be summarized as follows:

- The implementation of a magnetic field significantly impacts the velocity and thermal profiles of the nanofluid. The magnetic field generates a Lorentz force that opposes fluid motion, reducing velocity components in all directions. At the same time, the magnetic field enhances temperature distribution within the fluid due to the Joule heating effect.
- Increasing the medium's porosity results in a reduction in velocity across all directions, particularly near the rotating disk. The higher porosity increases the drag force, reducing the fluid's momentum and affecting the overall flow characteristics.
- The surface radial stress increases with increasing values of M, m and w_2 and decreases with increasing values of λ^* and ϑ. The surface resists torque in a reverse manner.
- The Hall current parameter increases the velocity of the hybrid nanofluid in all directions by altering the distribution of charged particles within the fluid. The velocity slip condition also reduces the interaction between the fluid and the disk surface, leading to thinner boundary layers and reduced momentum transfer.
- Prandtl number, Magnetic, nanoparticle and thermal radiation parameters significantly influence the temperature of the hybrid nanofluid.
- Thermophoresis parameter and mass-fraction of the Fe_3O_4 improves the temperature profiles in both hybrid fluids while thermal slip decreases the profiles.
- The Nusselt number significantly declines in response to elevations in N_t, N_{rnd}, α, w_2 and M, while it improves significantly as the Prandtl number increases.
- The concentration distribution of nanoparticles is influenced by parameters such as the Schmidt number, Brownian motion, thermal slip, and thermophoresis.
- Sherwood number increases with increasing values of N_b, w_2, α and M. It decreases as N_t and P_r increase.
- MWCNT outperforms SWCNT in terms of the thermal distribution and fluid motion.

References and Notes

1. H. Schlichting and K. Gersten, Boundary-Layer Theory. Springer-Verlag, Berlin, Heidelberg **(2016)**.
2. T. V. Kármán, *ZAMM-J. Appl. Math. Mech./Zeitschrift für Angew. Math. und Mechanik* 1, 233 **(1921)**.
3. F. Oluwaseun, S. Goqo, and H. Mondal, *Propulsion Power Res.* 13, 64 **(2024)**.
4. Kholoud Saad Albalawi, Mona Bin-Asfour, Badr Saad T. Alkahtani, J Madhu, RJ Punith Gowda, and R Naveen Kumar, *Numer Heat Transf, Part A: Appl.* 85, 1 **(2024)**.
5. K. B. Kasali and S. O. Ajadi, *J. Nanofluids* 14, 16 **(2025)**.
6. U. Farooq, A. Hassan, N. Fatima, M. Imran, M. S. Alqurashi, S. Noreen, A. Akgul, and A. Bariq, *Sci. Rep.* 13, 4679 **(2023)**.
7. E. M. Sparrow and J. L. Gregg. Mass Transfer, Flow, and Heat Transfer About a Rotating Disk, The American Society of Mechanical Engineers, USA **(1960)**.
8. M. Mustafa, *Int. J. Heat Mass Transf.* 108, 1910 **(2017)**.
9. C. Yin, L. Zheng, C. Zhang, and X. Zhang, *Propulsion Power Res.* 6, 25 **(2017)**.
10. M. Abbas, N. H. Siddiq, A. H. Majeed, and A. R. Ali, *J. Nanofluids* 14, 69 **(2025)**.
11. M. Muneeshwaran, G. Srinivasan, P. Muthukumar, and C.-C. Wang, *Int. Commun. Heat Mass Transf.* 125, 105341 **(2021)**.
12. J. Sarkar, P. Ghosh, and A. Adil, *Renew Sustain Energy Rev.* 43, 164 **(2015)**.
13. S. Suresh, K. P. Venkitaraj, P. Selvakumar, and M. Chandrasekar, *Exp. Therm. Fluid Sci.* 38, 54 **(2012)**.
14. S. M. S. Murshed, K. C. Leong, and C. Yang, *Appl. Therm. Eng.* 28, 2109 **(2008)**.
15. A. Ahmadian, M. Bilal, M. A. Khan, and M. I. Asjad, *Sci. Rep.* 10, 18776 **(2020)**.
16. A. Shahid, H. Huang, M. M. Bhatti, L. Zhang, and R. Ellahi, *Mathematics* 8, 380 **(2020)**.
17. K. B. Pavlov, *Magnitnaya Gidrodinamika* 4, 146 **(1974)**.
18. M. M. Rashidi, T. Hayat, E. Erfani, S. A. Mohimanian Pour, and A. A. Hendi, *Commun. Nonlin. Sci. Numer. Simul.* 16, 4303 **(2011)**.
19. T. Hayat, M. Waleed Ahmed Khan, M. Ijaz Khan, M. Waqas, and A. Alsaedi, *Phys. B: Condens. Matter* 538, 138 **(2018)**.

20. M. Ijaz Khan, F. Shah, T. Hayat, and A. Alsaedi, *Phys. A: Stat. Mech. Appl.* 527, 121154 (**2019**).
21. J. Ahmed, M. Khan, and L. Ahmad, *Phys. Lett. A* 383, 1300 (**2019**).
22. A. Raptis and C. Perdikis, *Int. J. Non-Linear Mech.* 41, 527 (**2006**).
23. M. Shoaib, M. A. Z. Raja, M. T. Sabir, K. S. Nisar, W. Jamshed, B. F. Felemban, and I. S. Yahia, *Coatings* 11, 1554 (**2021**).
24. S. A. Khan, I. M. Khan, T. Hayat, and A. Alsaedi, *Phys. Scr.* 94, 125009 (**2019**).
25. N. S. Anuar, N. Bachok, M. Turkyilmazoglu, N. M. Arifin, and H. Rosali, *Alex. Eng. J.* 59, 497 (**2020**).
26. B. Mahanthesh, B. J. Gireesha, I. L. Animasaun, T. Muhammad, and N. S. Shashikumar, *Phys. Scr.* 94, 085214 (**2019**).
27. T. Gul, A. Khan, M. Bilal, N. A. Alreshidi, S. Mukhtar, Z. Shah, and P. Kumam, *Sci. Rep.* 10, 8474 (**2020**).
28. O. D. Makinde and A. Aziz, *Int. J. Therm. Sci.* 50, 1326 (**2011**).
29. T. Hayat, S. A. Khan, M. Ijaz Khan, and A. Alsaedi, *Comput. Methods Programs Biomed.* 177, 57 (**2019**).
30. A. Kumar, R. Tripathi, and R. Singh, *J. Braz. Soc. Mech. Sci. Eng.* 41, 306 (**2019**).
31. M. I. Khan, S. Qayyum, T. Hayat, M. Waqas, M. I. Khan, and A. Alsaedi, *J. Mol. Liq.* 259, 274 (**2018**).
32. Y. -P. Lv, E. A. Algehyne, M. G. Alshehri, E. Alzahrani, M. Bilal, M. A. Khan, and M. Shuaib, *Sci. Rep.* 11, 8948 (**2021**).
33. F. Mabood, S. M. Ibrahim, M. M. Rashidi, M. S. Shadloo, and G. Lorenzini, *Int. J. Heat Mass Transf.* 93, 674 (**2016**).
34. S. Dinarvand, H. Berrehal, H. Tamim, G. Sowmya, S. Noeiaghdam, and M. Abdollahzadeh, *Results Eng.* 17, 100976 (**2023**).
35. M. P. Mkhatshwa and M. Khumalo, *Nonlin. Eng.* 12, 20220276 (**2023**).
36. M. P. Mkhatshwa, S. S. Motsa, M. S. Ayano, and P. Sibanda, *Case Stud. Therm. Eng.* 18, 100598 (**2020**).
37. M. P. Mkhatshwa, S. S. Motsa, and P. Sibanda, *Int. J. Comput. Methods* 18, 2150004 (**2021**).

ARTICLE